Available online at www.sciencedirect.com
SCIENCE DIRECT®
PERGAMON
International Journal of Heat and Mass Transfer 46 (2003) 2537–2545
International Journal of HEAT and MASS TRANSFER
www.elsevier.com/locate/ijhmt

Heat transfer and banks formation in a slag bath with embedded heat sources

Louis Gosselin, Marcel Lacroix *

Département de génie mécanique, Universitéde Sherbrooke, Sherbrooke, Que., Canada J1K 2R1

Received 29 March 2002; received in revised form 10 January 2003

Abstract

A study was conducted for the heat transfer and the formation of solid banks inside a bath of molten slag. This study is motivated by the need to predict the formation of a protective thermal barrier for the refractory brick walls inside smelting furnaces. A mathematical model for natural convection dominated solid liquid phase change with embedded heat sources is presented. A scale analysis is conducted yielding algebraic expressions for the steady-state minimal side bank thickness and location, molten volume fraction and average Nusselt number at the surface of the bath in terms of the Rayleigh number. The predictions of the scale analysis are validated with numerical results and their range of application are delineated.

1. Introduction

Electric arc furnaces (EAFs) are used for material processing that requires high powers and temperatures. Their main applications are the smelting of materials such as copper, nickel calcine, steel, pre-reduced iron ore and the melting/recycling of scrap metals from the automobile and metallurgical manufacturing industries [1]. A cross view of a typical electric arc smelting furnace is depicted in Fig. 1. The electrodes (only one electrode is shown here) are submerged in a bath of electrically conducting slag. The current is carried between the electrode tips in the slag to generate the heat (Joule effect) required for the smelting process. Heat losses are experienced at the surface of the slag and through the refractory brick walls.

Several studies have been conducted to predict the heat transfer and the flow circulation in the pools of EAFs [2–10]. The common objective of all these investigations is to gain basic understanding of the way in which energy transfer and utilisation takes place in the system so that the operational guidelines and the furnace designs are improved. Due to their complexity, solid/liquid phase change problems related to EAFs have received, however, comparatively little attention [11].

A fascinating melting/solidification phenomenon that arises in high temperature smelting furnaces is the formation of solid layers, called banks, on the inside surface of refractory brick walls (see Fig. 1). The presence of these banks is highly desirable as they serve as a protective thermal barrier for the refractory brick walls, thereby maintaining the integrity of the furnace and prolonging its active life. On the other hand, too thick a bank is detrimental to the furnace throughput as the volume available for smelting is reduced. Keeping banks of optimal size is therefore crucial in the safe and profitable operation of smelting furnaces. Unfortunately, due to the hostile conditions that prevail in the slag pool, probing their shape and their motion is a difficult task. The alternative is to predict their behaviour with mathematical models in terms of the furnace operating conditions.

The melting/solidification of the inner banks is dependent on the power transmitted to the slag pool, the heat transfer across the boundaries and the flow circulation in the slag bath. The flow circulation may be

* Corresponding author. Tel.: +1-819-821-8000; fax: +1-819-821-7163.
E-mail address: marcel.lacroix@gme.usherb.ca (M. Lacroix).

0017-9310/03/$ - see front matter © 2003 Elsevier Science Ltd. All rights reserved.
doi:10.1016/S0017-9310(03)00033-4

Nomenclature

A	coefficient
A_f	area of a control volume face f (m^2)
A_{mush}	constant (mushy zone)
B	coefficient
Bi	Biot number (hH_b/k)
c	heat capacity (J/kg K)
f_L	liquid fraction
g	gravitational acceleration (m/s^2)
H	height (m)
h	heat transfer coefficient (W/m^2 K)
i	sensible enthalpy (J/kg)
Δi	latent enthalpy (J/kg)
I	total enthalpy (J/kg)
k	thermal conductivity (W/m K)
Nu	Nusselt number ($q''/(k\Delta T/H_b)$)
p	pressure (Pa)
Pr	Prandtl number $\left(\frac{\mu/\rho}{\alpha}\right)$
q''	heat flux (W/m^2)
q'''	volumetric heat source (W/m^3)
Ra	Rayleigh number $\left(\frac{g\rho\beta q''' H_b^5}{k\alpha\mu}\right)$
s	bank thickness (m)
$S_x, S_y, S_q, S_{\Delta i}$	source terms
T	temperature (K)
t	time (s)
u	x velocity component (m/s)
v	y velocity component (m/s)
V	volume of the control volume (m^3)
W	width (m)
x	coordinate (m)
y	coordinate (m)

Greek symbols

α	thermal diffusivity (m^2/s)
β	thermal expansion coefficient (K^{-1})
ϕ	variable (u, v or i)
γ	constant
Γ	coefficient
ε	emissivity
θ	dimensionless temperature number $(\Delta T/(\alpha^2/H_b^3 g\beta))$
λ	latent heat of fusion (J/kg)
μ	viscosity (kg/m s)
ρ	density (kg/m^3)
σ	Stefan–Boltzmann constant (W/m^2 K^4)
χ	convergence criterion

Subscripts

w	wall
b	bath
up	upper bank or wall
down	bottom bank or wall
side	side bank
l	liquidus
s	solidus
e	electrode
f	face of a control volume
–	averaged value

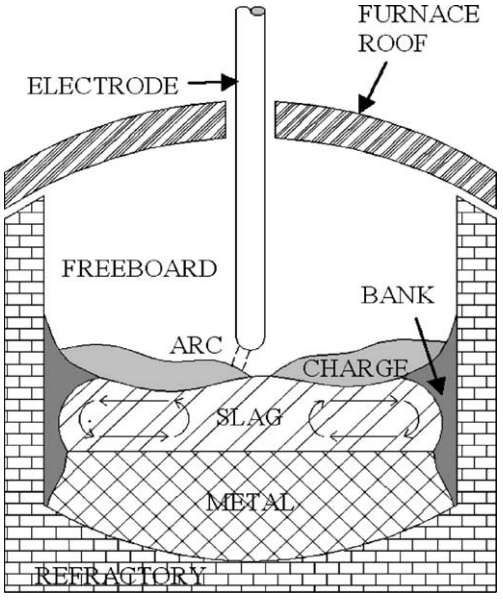

Fig. 1. Cross view of a typical smelting furnace.

caused by many factors such as the transfer of jet momentum at the bath surface, the electromagnetic forces induced by the passage of electric current, the natural convection resulting from thermal gradients and gas bubble driven circulation. To the authors' knowledge, the simultaneous effect of all these factors on the flow circulation has never been elucidated before let alone when melting and solidification of the slag banks take place at the inner walls.

The following investigation focuses on the solid–liquid phase change problem at the inner walls of a bath filled with slag. Heat transfer in the layer of molten metal lying underneath the slag is ignored and it is assumed that the principal driving force for the slag flow is limited to buoyancy. The momentum of the impinging jet, the effect of gas bubble and the electromagnetic forces are neglected. This scenario corresponds to an EAF for which the electrodes are submerged in the slag bath and operate at moderate power (less than 150 kW). Based on order-of-magnitude estimates, Szekely et al. [5] and Sheng et al. [7] have shown that in this case the electromagnetic stirring and the gas bubble circulation

are small compared to buoyancy driven flow. Moreover, the thermal energy transferred from the electrode to the bath is implemented in the computational model as volumetric heat sources distributed in the slag directly under the electrode [11].

This paper is a first step in the development of mathematical tools for predicting the formation of slag banks in EAFs. Its objective is to come up with simple algebraic formulae that provide basic information on the steady-state thermal behaviour of a slag bath with solidification at the surface of its inner walls. Key parameters such as the minimal side bank thickness, molten volume fraction and surface heat loss are reported in terms of the heat load to the bath. A scale analysis is first performed and its predictions are next confirmed with numerical simulations.

2. Physical model and numerical procedure

The physical system considered in the present study is illustrated in Fig. 2. A bath of height H_b and width $2W_b$ is filled with slag. The lateral wall of thickness W_w and the bottom wall of thickness H_w are made of refractory bricks. At time $t < 0$, the entire system is at a uniform temperature $T_i = T_l$. At time $t = 0$, heat is suddenly released from uniformly distributed sources in the slag pool underneath the electrode (region ABHG, Fig. 2) and, as a result, buoyancy driven flows are triggered. Heat is lost to the surroundings via the top surface of the pool (ABC) and via the lateral and bottom walls (CDEF). When the temperature of the slag in the vicinity of the brick walls falls below the liquidus, solid banks appear and grow in size until, at steady state, the heat lost at the boundaries matches the heat gained from the volumetric heat sources.

The dimensions of the system and the physical properties of the slag and of the refractory bricks are summarised in Tables 1–3 respectively. The mean temperature of the freeboard gas (the gas above the slag surface) is assumed to be constant ($T_{\infty,up} = 1500$ K) with an average heat transfer coefficient $h_{\infty,up} = 250$ W/m^2 K [9,10]. The outside surface of the bottom brick wall is air cooled with the air temperature set at $T_{\infty,down} = 300$ K and a heat transfer coefficient $h_{\infty,down} = 10$ W/m^2 K.

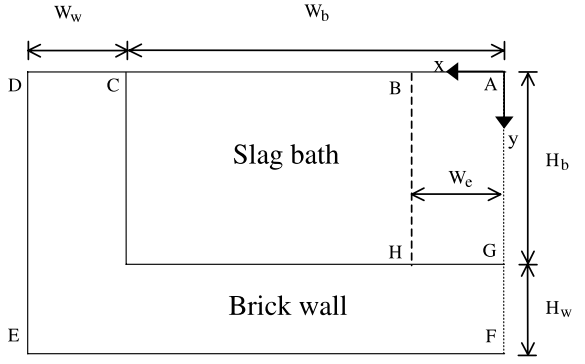

Fig. 2. Schematic representation of the slag bath and of the brick wall.

Table 1
Physical dimensions of the bath

W_e	0.3 m
W_b	2.6 m
W_w	0.7 m
H_b	1.0 m
H_w	1.0 m

Table 2
Thermophysical properties of the slag

ρ	3550 kg m^{-3}
c	1512 J kg^{-1} K^{-1}
λ	8.23×10^5 J kg^{-1}
k	4 W m^{-1} K^{-1}
μ	0.03 kg s^{-1} m^{-1}
solidus (T_s)	1842 K
liquidus (T_l)	1872 K
β	1.0×10^{-4} K^{-1}
T_{ref}	1872 K
ε	1

Table 3
Thermophysical properties of the refractory bricks

ρ	2851 kg m^{-3}
c	1100 J kg^{-1} K^{-1}
k	8 W m^{-1} K^{-1}
ε	1

The mathematical model for the heat transfer inside the slag bath rests on the following assumptions:

1. The depth of the bath (direction perpendicular to Fig. 2) is much larger than the plane dimensions (x–y) so that a two-dimensional analysis can be applied. Also, the fluid motion and heat transfer are symmetrical about the vertical centre line.
2. Circulation in the slag pool is caused by natural convection resulting from thermal gradients only.
3. The flow in the liquid pool is laminar, incompressible, and Newtonian and buoyancy is taken into account in the momentum equations via the Boussinesq approximation ($\beta \cdot \Delta T \ll 1$).

With the foregoing assumptions, the governing equations for the conservation of mass, momentum and energy are stated as

$$\frac{\partial u}{\partial x} + \frac{\partial v}{\partial y} = 0 \tag{1}$$

Table 4
Boundary conditions

Boundary	T	u	v
ABC	$-k_b \frac{\partial T}{\partial y} = h_{up}(T - T_{\infty,up}) + \varepsilon\sigma(T^4 - T^4_{\infty,up})$	$\frac{\partial u}{\partial y} = 0$	$v = 0$
CD	$\frac{\partial T}{\partial y} = 0$	–	–
DE	$-k_w \frac{\partial T}{\partial x} = h_{down}(T - T_{\infty,down}) + \varepsilon\sigma(T^4 - T^4_{\infty,down})$	–	–
EF	$-k_w \frac{\partial T}{\partial y} = h_{down}(T - T_{\infty,down}) + \varepsilon\sigma(T^4 - T^4_{\infty,down})$	–	–
FG	$\frac{\partial T}{\partial x} = 0$	–	–
GA	$\frac{\partial T}{\partial x} = 0$	$u = 0$	$\frac{\partial v}{\partial x} = 0$

$$\frac{\partial u}{\partial t} + u\frac{\partial u}{\partial x} + v\frac{\partial u}{\partial y} = \frac{\mu}{\rho}\left(\frac{\partial^2 u}{\partial x^2} + \frac{\partial^2 u}{\partial y^2}\right) - \frac{1}{\rho}\frac{\partial p}{\partial x} + S_x \tag{2}$$

$$\frac{\partial v}{\partial t} + u\frac{\partial v}{\partial x} + v\frac{\partial v}{\partial y} = \frac{\mu}{\rho}\left(\frac{\partial^2 v}{\partial x^2} + \frac{\partial^2 v}{\partial y^2}\right) - \frac{1}{\rho}\frac{\partial p}{\partial y} - g\beta(T - T_{ref}) + S_y \tag{3}$$

$$\frac{\partial i}{\partial t} + u\frac{\partial i}{\partial x} + v\frac{\partial i}{\partial y} = \alpha\left(\frac{\partial^2 i}{\partial x^2} + \frac{\partial^2 i}{\partial y^2}\right) + S_{\Delta i} + S_q \tag{4}$$

The corresponding boundary conditions are provided in Table 4. Solid–liquid phase change in the slag is treated with an enthalpy-porosity method [12]. In this method, the total enthalpy is split into sensible and latent heat components, i.e.,

$$I = i + \Delta i \tag{5}$$

where $\Delta i = f_L \lambda$. f_L represents the local liquid fraction and λ is the latent heat of fusion. The liquid fraction varies linearly between the solidus T_s and the liquidus T_l in the following manner:

$$f_L = \begin{cases} 0 & (T_s > T) \\ \frac{T - T_s}{T_l - T_s} & (T_s \leqslant T \leqslant T_l) \\ 1 & (T_l < T) \end{cases} \tag{6}$$

Therefore, the source term $S_{\Delta i}$ in the energy equation (4) becomes

$$S_{\Delta i} = -\left[\frac{\partial(\Delta i)}{\partial t} + u\frac{\partial(\Delta i)}{\partial x} + v\frac{\partial(\Delta i)}{\partial y}\right] \tag{7}$$

The liquid fraction is also used to drive the velocity components to zero in the solid phase of the slag and in the brick walls via the source terms S_x and S_y in the momentum equations (2) and (3):

$$S_i = \frac{1}{\rho}\frac{(1 - f_L)^3}{(f_L + \gamma)^2} A_{mush} u_i \tag{8}$$

with $A_{mush} = 10^6$ and $\gamma = 10^{-3}$. This numerical artefact can be viewed as a way of modelling the transition zone between the solid and liquid phases.

Finally, the source term S_q in the energy equation (4) is used to mimic the heat input from the electrode (region ABHG, Fig. 2):

$$S_q = \begin{cases} \left(\frac{q'''}{\rho}\right) & (0 \leqslant x \leqslant W_e,\ 0 \leqslant y \leqslant H_b) \\ 0 & \text{elsewhere} \end{cases} \tag{9}$$

The finite-difference equations are obtained on integrating the conservation equations, Eqs. (1)–(4), over each of the control volumes in the (x, y) plane. Second order finite differences are used for the diffusive terms while the power law scheme is retained for the convective terms [13]. An implicit Euler scheme is used for the time stepping procedure. The resulting finite difference equations for the general dependent variable ϕ at node P have the form

$$\sum_f^{N_{faces}} v_f \phi_f A_f = \sum_f^{N_{faces}} \Gamma_f (\nabla \phi_f)_n A_f + S_\phi V \tag{10}$$

The set of linearized equation (10) is then solved iteratively with a line-by-line tridiagonal matrix algorithm (TDMA). The SIMPLE algorithm is adopted for the pressure–velocity coupling. At a given time, convergence is declared when the dimensionless residuals for the mass and momentum conservation equations are less than 10^{-3} and the dimensionless residual for the energy equation is less than 10^{-6}. More stringent convergence criteria were employed, but the results, obtained after significantly longer computational times, did not show perceptible changes in the final solution.

The above computational model has been successfully tested and validated with experimental and numerical data for the melting and solidification of various substances [14,15]. As an example of validation, Fig. 3 compares the predicted solid–liquid interfaces with the experimental results reported by Gau and Viskanta [16] for the melting of gallium from a heated wall. The numerical simulation was carried out with a grid size of 42×32 control volumes and a time step of 5 s. Calculations performed with finer meshes and shorter time steps did not show perceptible differences with the present results.

3. Scale analysis

This section presents an order of magnitude analysis yielding algebraic relations for the steady-state minimal

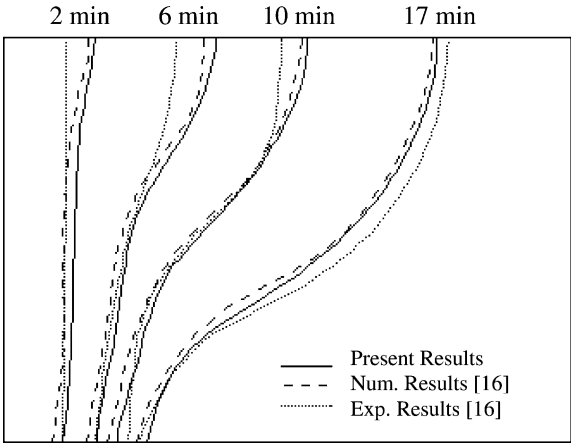

Fig. 3. Solid–liquid interface position and shape predicted and measured for a cavity filled with gallium.

side bank thickness and location, molten volume fraction and average Nusselt number at the top surface of the bath as a function of the Rayleigh number. In the following section, these relations will be validated with numerical results.

Inside the liquid zone of size $W_e \times H_b$ (region ABHG, Fig. 2), hereafter referred as the heating zone, the heat sources are uniformly distributed. It is assumed that in this region the buoyancy driven vertical flow velocities remain larger than the horizontal velocities. Neglecting the effect of thermal diffusion with respect to convection, the energy equation (4) then becomes

$$v\frac{\partial T}{\partial y} = \frac{q'''}{\rho c} \tag{11}$$

or, in terms of magnitude,

$$v\frac{\Delta T}{H_b} = \frac{q'''}{\rho c} \tag{12}$$

ΔT is the temperature difference $\Delta T = T - T_l$. In a similar manner, the momentum equation (3) leads to

$$\frac{v^2}{H_b} = \beta g \Delta T \tag{13}$$

Combining Eqs. (12) and (13), one obtains the following approximations for the vertical velocity and temperature in the heating zone:

$$\frac{|v|}{(\alpha/H_b)} = Ra^{1/3}Pr^{1/3} \tag{14}$$

$$\frac{\Delta T}{\left(\left(\frac{\alpha}{H_b}\right)^2 \frac{1}{g\beta H_b}\right)} = Ra^{2/3}Pr^{2/3} \tag{15}$$

where the Rayleigh and Prandtl numbers are defined as

$$Ra = \frac{g\rho\beta q''' H_b^5}{k\alpha\mu} \quad \text{and} \quad Pr = \frac{\mu/\rho}{\alpha} \tag{16}$$

At steady state, the banks inside the bath no longer change in size or in shape and the heat loss at the surface of the bath (line ABC, Fig. 2) may be evaluated with the help of thermal resistances, yielding

$$\frac{q''_{loss}}{\frac{k}{H_b}(T_L - T_{\infty,up})} = \left(\frac{1}{Bi_{up}} + \frac{\overline{s_{up}}}{H_b}\right)^{-1} \tag{17}$$

The Biot number is defined here as

$$Bi_{up,down} = \frac{h_{up,down}H_b}{k} \tag{18}$$

The heat transferred to the banks comes from the hot fluid flowing along the solid–liquid interface, i.e., $q''_{gain} \sim W_b^{-1}(\rho W_e|v|)(c\Delta T)$. Then, from Eqs. (14) and (15),

$$\frac{q''_{gain}}{\frac{k}{H_b}(T_L - T_{\infty,up})} = \left(\frac{W_e}{W_b}\right)\frac{RaPr}{\theta_{up}} \tag{19}$$

where the dimensionless number $\theta_{up,down}$ is defined as

$$\theta_{up,down} = \frac{(T_L - T_{\infty,up,down})}{\left(\frac{\alpha}{H_b}\right)^2 \frac{1}{g\beta H_b}} \tag{20}$$

Combining Eqs. (17) and (19), the mean thickness of the bank at the surface of the pool is then given by

$$\frac{\overline{s_{up}}}{H_b} = \left(\frac{W_b}{W_e}\right)\frac{\theta_{up}}{RaPr} - \frac{1}{Bi_{up}} \tag{21}$$

In a similar fashion, the mean thickness of the bank sitting at the bottom of the pool is approximated by

$$\frac{\overline{s_{down}}}{H_b} = \left(\frac{W_b}{W_e}\right)\frac{\theta_{down}}{RaPr} - \frac{1}{Bi_{down}} - \frac{kH_w}{k_w H_b} \tag{22}$$

As one moves away from the heating zone along the x axis, the top and bottom banks increase in size. In the range of the operating conditions considered in the present study, both banks eventually merge on the left vertical wall. As depicted in Fig. 4, the thickness of the side bank at this point is minimal and it represents the most vulnerable spot on the lateral brick wall. From a practical point of view, predicting the location H_{side} and the thickness s_{side} of the side bank at this point is therefore essential for the safe operation of the furnace. For the sake of the present analysis, it is assumed that the thickness of the top and bottom banks increases linearly in the x direction (Fig. 4). Then, for the top bank,

$$\frac{s_{up}(x)}{H_b} = \frac{(H_b - H_{side})}{(W_b - s_{side})}\frac{x}{H_b} \quad \left(0 \leqslant \frac{x}{H_b} \leqslant \frac{W_b - s_{side}}{H_b}\right) \tag{23}$$

which yields an average value of

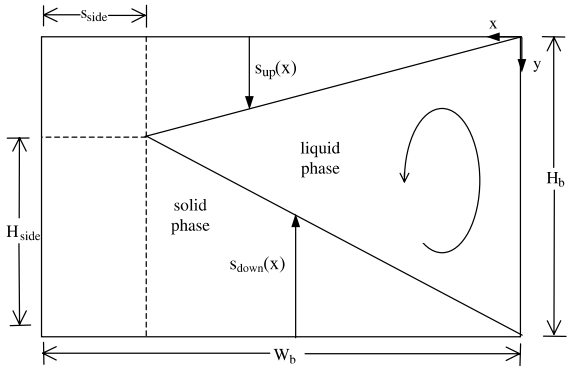

Fig. 4. Schematic representation of the bath in the presence of a lateral bank. The top and bottom banks are assumed to increase linearly with x, Eq. (23).

$$\frac{\overline{s_{\mathrm{up}}}}{H_{\mathrm{b}}}=\frac{1}{2}\left(1-\frac{H_{\mathrm{side}}}{H_{\mathrm{b}}}\right) \tag{24}$$

Similarly, for the bottom bank, one finds

$$\frac{\overline{s_{\mathrm{down}}}}{H_{\mathrm{b}}}=\frac{1}{2}\left(\frac{H_{\mathrm{side}}}{H_{\mathrm{b}}}\right) \tag{25}$$

These average values for the thickness of the top and bottom banks are consistent with those of Eqs. (21) and (22). Combining Eq. (21) with (24) and Eq. (22) with (25) and rearranging, one obtains the following relations for the minimal side bank thickness s_{side} and location H_{side}:

$$\frac{s_{\mathrm{side}}}{W_{\mathrm{b}}}=1-\frac{W_{\mathrm{e}}}{W_{\mathrm{b}}}\frac{RaPr}{\theta_{\mathrm{up}}+\theta_{\mathrm{down}}}\left[\frac{1}{2}+\frac{1}{Bi_{\mathrm{up}}}+\frac{1}{Bi_{\mathrm{down}}}+\frac{kH_{\mathrm{w}}}{k_{\mathrm{w}}H_{\mathrm{b}}}\right] \tag{26}$$

$$\frac{H_{\mathrm{side}}}{H_{\mathrm{b}}}=\left(\frac{\theta_{\mathrm{down}}-\theta_{\mathrm{up}}}{\theta_{\mathrm{down}}+\theta_{\mathrm{up}}}\right)\left(1+\frac{1}{Bi_{\mathrm{down}}}+\frac{kH_{\mathrm{w}}}{k_{\mathrm{w}}H_{\mathrm{b}}}+\frac{1}{Bi_{\mathrm{up}}}\right)-\frac{1}{Bi_{\mathrm{down}}}-\frac{kH_{\mathrm{w}}}{k_{\mathrm{w}}H_{\mathrm{b}}}+\frac{1}{Bi_{\mathrm{up}}}+\frac{1}{2} \tag{27}$$

Both Eqs. (26) and (27) are based on a characteristic length scale of $W_{\mathrm{b}}-s_{\mathrm{side}}$ for the liquid bath width.

The second parameter of interest is the molten volume fraction in the bath. It is defined as

$$\overline{f_{\mathrm{L}}}=\frac{1}{H_{\mathrm{b}}W_{\mathrm{b}}}\int_0^{H_{\mathrm{b}}}\int_0^{W_{\mathrm{b}}}f_{\mathrm{L}}(x,y)\,\mathrm{d}x\,\mathrm{d}y \tag{28}$$

This parameter provides information on the overall volume occupied by the banks inside the bath. A fraction of 1 indicates that the entire bath if filled with liquid metal while a fraction of 0 means that the entire bath is frozen solid. When convection heat transfer inside the liquid pool dominates, i.e., for large values of the Rayleigh number (Eq. (16)), the hot slag flowing along the top surface impinges on the lateral wall thereby preventing the direct formation of a side bank. As a result, banks appear and grow in size mainly from the top surface where the heat loss to the freeboard is significant (compared to the heat losses through the side and bottom walls) and from the bottom wall where the slag temperature sinks below the liquidus. Then, from Eqs. (21) and (22), the molten volume fraction (28) may be approximated by $\overline{f_{\mathrm{L}}}\sim 1-\frac{\overline{s_{\mathrm{up}}}+\overline{s_{\mathrm{down}}}}{H_{\mathrm{b}}}$, yielding

$$\overline{f_{\mathrm{L}}}=\begin{cases}0 & (Ra<Ra_0)\\ \frac{1}{Ra}\left[-\left(\frac{W_{\mathrm{b}}}{W_{\mathrm{e}}}\right)\frac{\theta_{\mathrm{up}}+\theta_{\mathrm{down}}}{Pr}\right] & \\ \quad+\left[1+\frac{1}{Bi_{\mathrm{up}}}+\frac{1}{Bi_{\mathrm{down}}}+\frac{kH_{\mathrm{w}}}{k_{\mathrm{w}}H_{\mathrm{b}}}\right] & (Ra_0\leqslant Ra\leqslant Ra_1)\\ 1 & (Ra>Ra_1)\end{cases} \tag{29}$$

where

$$Ra_0=\frac{\theta_{\mathrm{up}}+\theta_{\mathrm{down}}}{\left(\frac{W_{\mathrm{e}}}{W_{\mathrm{b}}}\right)Pr\left(1+\frac{1}{Bi_{\mathrm{up}}}+\frac{1}{Bi_{\mathrm{down}}}+\frac{kH_{\mathrm{w}}}{k_{\mathrm{w}}H_{\mathrm{b}}}\right)} \tag{30}$$

and

$$Ra_1=\frac{\theta_{\mathrm{up}}+\theta_{\mathrm{down}}}{\left(\frac{W_{\mathrm{e}}}{W_{\mathrm{b}}}\right)Pr\left(\frac{1}{Bi_{\mathrm{up}}}+\frac{1}{Bi_{\mathrm{down}}}+\frac{kH_{\mathrm{w}}}{k_{\mathrm{w}}H_{\mathrm{b}}}\right)} \tag{31}$$

On the other hand, when conduction heat transfer prevails inside the liquid pool, i.e., for small Rayleigh numbers (Eq. (16)), the buoyancy driven flows are weak and a side bank may appear and grow in size simultaneously along with the top and bottom banks. Combining Eq. (29) with Eqs. (24)–(27) and rearranging, one obtains

$$\overline{f_{\mathrm{L}}}=\frac{1}{2}\frac{W_{\mathrm{e}}}{W_{\mathrm{b}}}\frac{RaPr}{\theta_{\mathrm{up}}+\theta_{\mathrm{down}}}\left[\frac{1}{2}+\frac{1}{Bi_{\mathrm{up}}}+\frac{1}{Bi_{\mathrm{down}}}+\frac{kH_{\mathrm{w}}}{k_{\mathrm{w}}H_{\mathrm{b}}}\right] \tag{32}$$

Both Eqs. (29) and (32) will later be compared to the numerical results in order to define precisely their range of application in terms of the magnitude of the Rayleigh number Ra.

The third parameter of interest is the average Nusselt number at the top surface of the bath. It provides information on the magnitude of the heat loss from the top surface to the freeboard. For convection dominated heat transfer, the average Nusselt number is evaluated by combining Eqs. (17) and (21) yielding

$$\overline{Nu}_{\mathrm{up}}=\frac{\overline{q''}_{\mathrm{loss}}}{\frac{k}{H_{\mathrm{b}}}(T_{\mathrm{L}}-T_{\infty,\mathrm{up}})}=\left(\frac{W_{\mathrm{e}}}{W_{\mathrm{b}}}\right)\frac{RaPr}{\theta_{\mathrm{up}}} \tag{33}$$

If conduction is the prevailing mechanism of heat transfer in the bath, i.e., for small Rayleigh numbers, the heat released from the sources is mainly transferred to the surroundings via two thermal resistances,

$$\frac{T_{\mathrm{in}}-T_{\infty,\mathrm{up}}}{\frac{H_{\mathrm{b}}}{k}+\frac{1}{h_{\mathrm{up}}}}+\frac{T_{\mathrm{in}}-T_{\infty,\mathrm{down}}}{\frac{H_{\mathrm{b}}}{k}+\frac{1}{h_{\mathrm{down}}}+\frac{H_{\mathrm{w}}}{k_{\mathrm{w}}}}=\frac{q'''H_{\mathrm{b}}W_{\mathrm{e}}}{W_{\mathrm{b}}} \tag{34}$$

Table 5
Dimensionless numbers

	Number	Value
Pr	$\frac{\mu/\rho}{\alpha}$	11.3
Bi_{up}	$\frac{h_{\mathrm{up}}H_{\mathrm{b}}}{k}$	200.0
Bi_{down}	$\frac{h_{\mathrm{down}}H_{\mathrm{b}}}{k}$	57.8
θ_{up}	$(T_{\mathrm{L}}-T_{\infty,\mathrm{up}})\left[\left(\frac{\alpha}{H_{\mathrm{b}}}\right)^2\frac{1}{g\beta H_{\mathrm{b}}}\right]^{-1}$	6.59×10^{11}
θ_{down}	$(T_{\mathrm{L}}-T_{\infty,\mathrm{down}})\left[\left(\frac{\alpha}{H_{\mathrm{b}}}\right)^2\frac{1}{g\beta H_{\mathrm{b}}}\right]^{-1}$	2.78×10^{12}
Ra	$\frac{g\rho\beta q''' H_{\mathrm{b}}^5}{k\alpha\mu}$	1.9×10^{12}–1.9×10^{13}

T_{in} is a characteristic temperature inside the heating zone. Rearranging Eq. (34) for T_{in} and keeping in mind that the first term on the left-hand side represents the heat lost at the top surface, one finds the following expression for the average Nusselt number for small Rayleigh numbers:

$$\overline{Nu}_{\mathrm{up}}=\frac{H_{\mathrm{b}}}{W_{\mathrm{b}}}\left(1-\frac{\theta_{\mathrm{down}}}{\theta_{\mathrm{up}}}\right)\frac{\left(1+\frac{1}{Bi_{\mathrm{down}}}+\frac{H_{\mathrm{w}}k}{k_{\mathrm{w}}H_{\mathrm{b}}}\right)}{\left(2+\frac{1}{Bi_{\mathrm{up}}}+\frac{1}{Bi_{\mathrm{down}}}+\frac{H_{\mathrm{w}}k}{k_{\mathrm{w}}H_{\mathrm{b}}}\right)}\times\left\{\frac{1}{\left(1+\frac{1}{Bi_{\mathrm{up}}}\right)}+\frac{W_{\mathrm{e}}}{H_{\mathrm{b}}}\frac{RaPr}{\theta_{\mathrm{down}}-\theta_{\mathrm{up}}}\right\}\tag{35}$$

Once again, in the following section, Eqs. (33) and (35) for the Nusselt number will be tested against the numerical predictions.

The dimensionless numbers were estimated with the physical dimensions and properties provided in Tables 1–3. They are reported in Table 5. The Biot numbers in Table 5 were estimated with an overall heat transfer coefficient that takes into account the radiation effect, i.e.,

$$h_{\mathrm{up,down}}\sim h_{\mathrm{up,down}}^{\mathrm{conv}}+\frac{1}{2}\sigma\varepsilon(T_{\mathrm{l}}+T_{\infty,\mathrm{up,down}})(T_{\mathrm{l}}^2+T_{\infty,\mathrm{up,down}}^2)\tag{36}$$

The heat load to the bath varies from 15 to 150 kW yielding Rayleigh numbers ranging from 1.9×10^{12} to 1.9×10^{13}.

4. Results and discussion

All simulations reported here were carried out until the steady-state regime was reached. Steady state is declared when the following condition is satisfied:

$$\left|\frac{\int_{\mathrm{ABCDEF}}q''\,\mathrm{d}l-q'''W_{\mathrm{e}}H_{\mathrm{b}}}{q'''W_{\mathrm{e}}H_{\mathrm{b}}}\right|\leqslant\chi\tag{37}$$

where $\chi=5\times10^{-3}$. Calculations were performed on a SGI ORIGIN 2000 computer and the CPU time for a typical run ranged from 12 to 24 h depending on the grid size and the time step. Every time the Rayleigh number was changed, the accuracy of the numerical predictions was checked by performing a grid refinement study. As a result, grid sizes stretch from 50×30 control volumes to 95×70 control volumes. The effect of the time step to reach a steady-state solution was also investigated and, in general, a time step of 100 seconds was retained. Calculations performed with smaller time steps yielded the very same steady-state solution after, however, considerably longer computational times.

Fig. 5 exemplifies the effect of the Rayleigh number on the minimal side bank thickness s_{side} and location H_{side}. Each datum on this figure is the result of a full simulation. The numerical results are also compared with the predictions of the scale analysis from the previous section. It was shown, in Eq. (26), that the minimal thickness of the side bank is a linear function of the Rayleigh number, i.e.,

$$\frac{s_{\mathrm{side}}}{W_{\mathrm{b}}}\sim B-ARa\tag{38}$$

where B and A are constants. For the present problem, the scale analysis reveals that $B\approx1$ and $A\approx3.9\times10^{-12}$. A least-square fit of the numerical predictions yielded

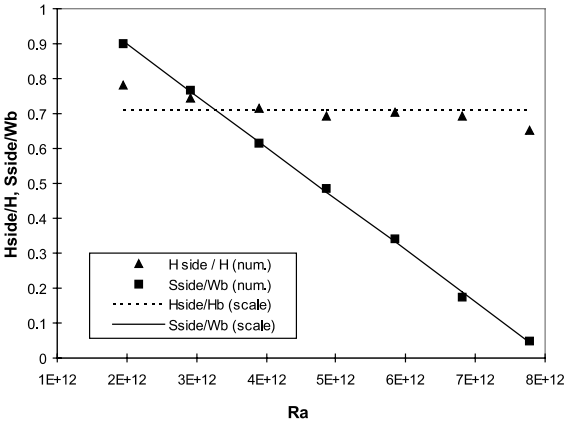

Fig. 5. Minimal thickness of the side bank and location versus Rayleigh number.

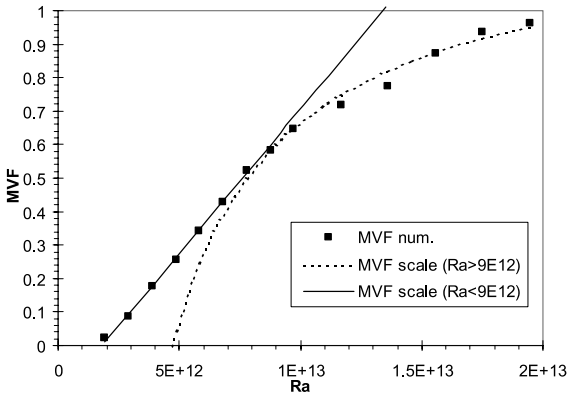

Fig. 6. Molten volume fraction versus Rayleigh number.

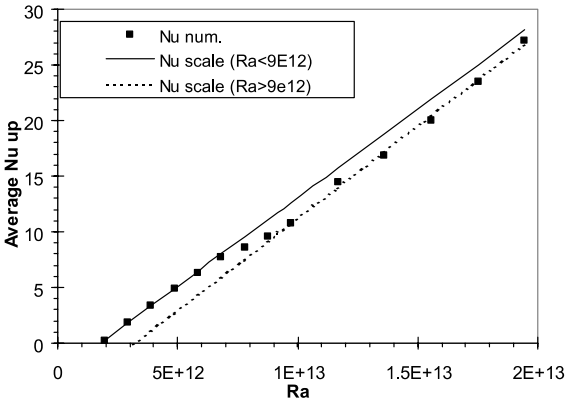

Fig. 7. Average Nusselt number at the surface of the bath versus Rayleigh number.

$B = 1.19$ and $A = 14.7 \times 10^{-12}$. On the other hand, Eq. (27) dictates that the location for the minimum thickness of the side bank remains independent of the Rayleigh number. This result is also confirmed by the numerical predictions reported in Fig. 5.

Table 6
Scale analysis and numerical results

Scale analysis relations	Predictions of the scale analysis	Numerical results
$\frac{s_{\text{side}}}{W_b} = B - ARa$ (Eq. (26))	$A = \frac{W_e}{W_b}\frac{Pr}{\theta_{up}+\theta_{down}}\left[\frac{1}{2}+\frac{1}{Bi_{up}}+\frac{1}{Bi_{down}}+\frac{kH_w}{k_wH_b}\right] \sim 3.9\times10^{-12}$	$A = 14.73\times10^{-12}$
	$B \sim 1$	$B = 1.19$
$\frac{H_{\text{side}}}{H} = A$ (Eq. (27))	$A = \left(\frac{\theta_{down}-\theta_{up}}{\theta_{down}+\theta_{up}}\right)\left(1+\frac{1}{Bi_{down}}+\frac{kH_w}{k_wH_b}+\frac{1}{Bi_{up}}\right) -\frac{1}{Bi_{down}}-\frac{kH_w}{k_wH_b}+\frac{1}{Bi_{up}}+\frac{1}{2}\sim 0.9$	$A = 0.71$
$\overline{f_L} \sim \frac{-A}{Ra}+B$ $(Ra \geqslant 9\times10^{12})$ (Eq. (29))	$A = \left(\frac{W_b}{W_e}\right)\frac{\theta_{up}+\theta_{down}}{Pr} \sim 2\times10^{12}$	$A = 5.9\times10^{12}$
	$B = \left[1+\frac{1}{Bi_{up}}+\frac{1}{Bi_{down}}+\frac{kH_w}{k_wH_b}\right]\sim 1.5$	$B = 1.25$
$\overline{f_L} \sim ARa - B$ $(Ra \geqslant 9\times10^{12})$ (Eq. (32))	$A = \frac{1}{2}\frac{W_e}{W_b}\frac{Pr}{\theta_{up}+\theta_{down}}\left[\frac{1}{2}+\frac{1}{Bi_{up}}+\frac{1}{Bi_{down}}+\frac{kH_w}{k_wH_b}\right]\sim 2.0\times10^{-13}$	$A = 0.86\times10^{-13}$
	$B \sim 0$	$B = 0.16$
$\overline{Nu}_{up} \sim ARa - B$ $(Ra \geqslant 9\times10^{12})$ (Eq. (33))	$A = \left(\frac{W_e}{W_b}\right)\frac{Pr}{\theta_{up}} \sim 2.1\times10^{-12}$	$A = 1.7\times10^{-12}$
	$B \sim 0$	$B = 5.3$
$\overline{Nu}_{up} \sim ARa - B$ $(Ra \leqslant 9\times10^{12})$ (Eq. (35))	$A = \frac{\left(1-\frac{\theta_{down}}{\theta_{up}}\right)\left(1+\frac{1}{Bi_{down}}+\frac{H_wk}{k_wH_b}\right)}{\left(2+\frac{1}{Bi_{up}}+\frac{1}{Bi_{down}}+\frac{H_wk}{k_wH_b}\right)}\times\frac{W_e}{W_b}\left(\frac{Pr}{\theta_{down}-\theta_{up}}\right)\sim 1.2\times10^{-12}$	$A = 1.6\times10^{-12}$
	$B = \frac{\frac{H_b}{W_b}\left(1-\frac{\theta_{down}}{\theta_{up}}\right)\left(1+\frac{1}{Bi_{down}}+\frac{H_wk}{k_wH_b}\right)}{\left(2+\frac{1}{Bi_{up}}+\frac{1}{Bi_{down}}+\frac{H_wk}{k_wH_b}\right)\left(1+\frac{1}{Bi_{up}}\right)}\sim 0.7$	$B = 2.84$

The variation of the mean molten volume fraction with respect to the Rayleigh number is depicted in Fig. 6. As predicted by the scale analysis (Eq. (29)), for convection dominated heat transfer in the melt,

$$\overline{f_L} \sim \frac{-A}{Ra} + B \tag{39}$$

The numerical simulations show that this expression holds for $Ra \geqslant 9 \times 10^{12}$. The predictions of the scale analysis are $A \approx 2 \times 10^{12}$ and $B \approx 1.5$ and the numerical results yield $A = 5.90 \times 10^{12}$ and $B = 1.25$. On the other hand, when conduction heat transfer prevails in the melt, i.e., for $Ra \leqslant 9 \times 10^{12}$, the scale analysis (Eq. (32)) reveals that

$$\overline{f_L} \sim ARa - B \tag{40}$$

with $A \approx 2.0 \times 10^{-13}$ and $B \approx 0$. The numerical predictions are $A = 0.86 \times 10^{-13}$ and $B = 0.16$. Incidentally, it is interesting to note that Eq. (39) is valid for $\overline{f_L} \leqslant 0.5$ and Eq. (40) for $\overline{f_L} \geqslant 0.5$.

The effect of Ra on the average Nusselt number at the surface of the bath is illustrated in Fig. 7. Once again, the scale analysis is in good agreement with the numerical results. Eqs. (33) and (35) show that

$$\overline{Nu}_{up} \sim ARa - B \tag{41}$$

For $Ra \geqslant 9 \times 10^{12}$, the scale analysis yields $A \approx 2.1 \times 10^{-12}$ and $B \approx 0$ compared to $A = 1.65 \times 10^{-12}$ and $B = 5.3$ for the numerical simulations. For $Ra \leqslant 9 \times 10^{12}$, the scale analysis shows $A \approx 1.2 \times 10^{-12}$ and $B \approx 0.7$ and the numerical predictions reveal $A = 1.59 \times 10^{-12}$ and $B = 2.8$.

For convenience, the results reported in Eqs. (38)–(41) are gathered in Table 6.

5. Concluding remarks

A study was conducted for the natural convection dominated heat transfer and the formation of solid banks inside a bath of molten slag. A scale analysis of the problem yielded simple algebraic expressions, later validated with numerical simulations, for the steady-state minimal thickness and location of the of the side bank, for the molten volume fraction and for the average Nusselt number at the surface of the bath in terms of the Rayleigh number.

Acknowledgements

The authors gratefully acknowledge the financial support of the Natural Sciences and Engineering Research Council of Canada.

References

[1] M. Orfeuil, Electric Process Heating, Battelle Press, 1987.
[2] W.D. Heiss, Fields, power density and effective resistance in the electrode and furnace of an electric smelter, Elektrowärme Int. 39 (1981) 243–249.
[3] T. Ma, J.D. Lavers, A finite element iterative simulation of couples electrothermal effects in an electric smelting furnace, IEE Trans. Magn. Mag-21 (6) (1985) 2416–2419.
[4] T. Ma, J.D. Lavers, A finite-element package for the analysis of electromagnetic forces and power in an electric smelting furnace, IEEE Trans. Ind. Appl. IA-22 (4) (1986) 578–585.
[5] J. Szekely, J. McKelliget, M. Choudhary, Heat-transfer fluid flow and bath circulation in electric-arc furnaces and dc plasma furnaces, Ironmaking Steelmaking 10 (4) (1983) 169–179.
[6] Y.Y. Sheng, G.A. Irons, D.G. Tisdale, Transport phenomena in electric smelting of nickel matte: Part I. Electric potential distribution, Metall. Mater. Trans. B 29B (1998) 77–83.
[7] Y.Y. Sheng, G.A. Irons, D.G. Tisdale, Transport phenomena in electric smelting of nickel matte: Part II. Mathematical modeling, Metall. Mater. Trans. B 29B (1998) 85–94.
[8] M.A. Ramirez, G. Trapaga, J. Alexis, P. Jönsson, Effects of the arc, slag and bottom bubbling of argon on the fluid flow and heat transfer of a dc EAF bath (Part II), in: Electric Furnace Conference Proceedings, 1999, pp. 751–761.
[9] J. Alexis, M. Ramirez, G. Trapaga, P. Jönsson, Modeling of heat transfer from an electric arc—a simulation of heating (Part I), in: Electric Furnace Conference Proceedings 1999, pp. 279–287.
[10] J. Alexis, M. Ramirez, G. Trapaga, P. Jönsson, Modeling of a dc electric arc furnace-heat transfer from the arc, ISIJ Int. J. 40 (11) (2000) 1089–1097.
[11] A.H. Castillejos, F.A. Acosta, M.A. Pedrosa, M.A. Herrera, A thermal study to improve the lifetime of Billet-type bottom electrodes of dc electric arc furnaces: Part I—Melting of the metallic charge, ISS Trans. (2001) 61–71.
[12] A.D. Brent, V.R. Voller, J. Reid, Enthalpy-porosity technique for modeling convection–diffusion phase change: application to the melting of a pure metal, Numer. Heat Transfer 13 (1988) 297–318.
[13] S.V. Patankar, Numerical Heat Transfer and Fluid Flow, Hemisphere Publishing, Washington, DC, 1980.
[14] O. Bertrand, B. Binet, H. Combeau, S. Couturier, Y. Delannoy, D. Gobin, M. Lacroix, P. Le Quéré, M. Medale, J. Mencinger, G. Vieira, Melting driven by natural convection, a comparison exercise: first results, Int. J. Therm. Sci. 38 (1999) 5–26.
[15] B. Binet, M. Lacroix, Numerical study of natural convection dominated melting inside uniformly and discretely heated rectangular cavities, Numer. Heat Transfer A 33 (2) (1998) 207–224.
[16] C. Gau, R. Viskanta, Melting and solidification of a pure metal on a vertical wall, J. Heat Transfer 108 (1986) 174–181.